Interface perpendicular magnetic anisotropy in heterostructures consisting of CoFeB and conductive rock-salt Li-Ti-O

Hiroki Koizumi[1,2,*], Zhenchao Wen[1], Jun Uzuhashi[1], Tadakatsu Ohkubo[1], Hiroaki Sukegawa[1,*] and Seiji Mitani[1,3]

[1] National Institute for Materials Science (NIMS), Tsukuba 305-0047, Japan
[2] Center for Science and Innovation in Spintronics (CSIS), Tohoku University, Sendai 980-8577, Japan
[3] Graduate School of Science and Technology, University of Tsukuba, Tsukuba 305-8577, Japan

E-mail: sukegawa.hiroaki@nims.go.jp, hiroki.koizumi.d7@tohoku.ac.jp

Received xxxxxx
Accepted for publication xxxxxx
Published xxxxxx

Abstract

We investigated interface perpendicular magnetic anisotropy (PMA) in magnetic heterostructures consisting of ferromagnetic metal CoFeB and conductive rock-salt Li-Ti-O (LTO) layers, which can be classified into an unconventional group different from metallic multilayers and tunnel junctions. The rock-salt structure was confirmed by reflection high-energy electron diffraction for the 5 nm thick LTO layers epitaxially grown on a MgO(001) buffer layer. Interface PMA was clearly observed for the LTO/CoFeB heterostructures with post-annealing above 250˚C, and the effective PMA energy density reached 1.18 Merg/cm^3 with post-annealing at 300˚C. The LTO layer thickness dependence of the resistance area product and tunnel magnetoresistance showed a clear difference in transport properties between the present LTO/CoFeB and the conventional MgO/CoFeB heterostructures, as evidence for the electrical conductivity of LTO in the LTO/CoFeB heterostructure. The conductive LTO can be used as a new building block for a PMA heterostructure for spintronic devices.

Keywords: Li-Ti-O, conductive oxide, perpendicular magnetic anisotropy, interface, tunnel magnetoresistance

* Author to whom any correspondence should be addressed.

1. Introduction

Perpendicular magnetic anisotropy (PMA), which has been found for various materials and is currently used for several applications, is one of the most important properties of ferromagnetic thin films[1-4]. While the mechanism of PMA for most of cases is simply attributable to a spin-orbit coupling, electric quadrupole may also play a crucial role for PMA [5-9]. Nowadays, magneto-resistive random-access memory (MRAM) devices with a high density and a low switching current have been developed using interface PMA [10-12], which has been found for heterostructures consisting of a ferromagnetic metal and an insulating oxide such as W/CoFeB/MgO [13-15], CoFeAl/MgO [16], Fe/MgO [17]

and Fe/$MgAl_2O_4$ [18]. Such PMA induced at oxide interfaces is different in the mechanism from the PMA observed in metallic multilayers such as Co/Pt [19]. Interestingly, interface PMA has been demonstrated even at transition metal oxide interfaces such as TiO_x/CoFeB [20], NiO/Fe[21], and CrO_x/Fe [22].

There are some important related issues in ferromagnetic metal/oxide heterostructures, particularly for spintronic application. Heterostructures consisting of CoFe(B) and MgO have long attracted much interest for the high tunnel magnetoresistance (TMR) ratio [23,24], as well as the spin transfer torque and the voltage-controlled magnetic anisotropy effect (VCMA) [11,25]. For practical applications of MRAMs, one of the major challenges is to enhance interface PMA, so that multiple MgO interfaces are considered [26–28]. Although the use of multiple oxide layer interfaces is a promising way, there exists a risk of substantial increase in device resistance and therefore one may wonder whether the insulating oxide in the interface PMA heterostructures can be replaced with a conductive oxide that is free from the problem.

Lithium titanate $LiTi_2O_4$ is known as a conductive oxide with a normal spinel structure with a space group of $Fd\bar{3}m$ [29]. Lithium titanate can vary the Li composition over a wide range while maintaining cubic crystals, e.g., spinel $LiTi_2O_4$ (a = 0.841 nm), spinel $Li_4Ti_5O_{12}$ (a = 0.836 nm), and a rock-salt $Li_7Ti_5O_{12}$ ($2a$ = 0.835 nm) [29–31]. This means that the lattice constant can be tuned by changing the chemical composition, similar to spinel $MgAl_2O_4$ [32]. Moreover, the resistivity can also be tuned by the composition. Since electrical resistivity of the Li-Ti-O (LTO) system can be low compared with conventional MgO, LTO will be suitable for an oxide layer to introduce interface PMA without increasing the device resistance. Note that low resistance is a common demand for spintronic devices. In addition, if interface PMA is obtained in the LTO system, the tunability of lattice constant and resistivity is possibly beneficial for a variety of device applications. In this study, we investigated interface PMA in heterostructures consisting of a CoFeB and rock-salt LiTiO. Substantial interface PMA with effective PMA energy densities up to 1.18 Merg/cm^3 was demonstrated, independent of the electrically conductive properties of the LTO layer. The PMA heterostructures with a conductive oxide LTO layer can be regarded as a new PMA system for spintronic devices.

2. Experiment

Figure 1 shows schematic multilayer structures consisting of CoFeB and LTO to investigate PMA and TMR properties. All layers were grown on MgO(001) substrates using a radio-frequency (RF) magnetron sputtering system with a base pressure less than 1×10^{-6} Pa.

We have fabricated two series of multilayers, as shown in Fig. 1. The first multilayer is prepared for evaluating interface PMA as schematically shown in the left side of Fig. 1. A stack structure of MgO substrate/Cr buffer (50 nm)/MgO (1 nm)/LTO (5 nm)/$Co_{20}Fe_{60}B_{20}$ (CoFeB) (t_{CFB} = 0.8, 1.1, 1.4, 1.7, 2.2, 2.7 nm)/W (0.3 nm)/Ta (1.0 nm)/Ru cap (15 nm) was deposited at room temperature (RT). Prior to the deposition, the substrate was annealed at 800°C to clean its surface. The Cr buffer layer was deposited with a substrate temperature of 150°C, and the layer was post-annealed at 800°C to improve the Cr flatness and crystallinity. The MgO and LTO layers were deposited with an Ar gas pressure of 10 mTorr (1.33 Pa) from a MgO and a $Li_4Ti_5O_{12}$ stoichiometric sintered target, respectively. Epitaxial growth with (001) orientation was achieved from the Cr buffer to the LTO layer due to their good lattice matching. After deposition, *ex-situ* post-annealing (PA) was performed at various temperatures.

The second stack is an orthogonal magnetization type magnetic tunnel junction (MTJ) to evaluate magonetotransport properties through the MgO/LTO barrier, as shown in the right side of Fig. 1. A MTJ stack of MgO(001) substrate/Cr buffer (50 nm)/Fe (5 nm)/MgO (1 nm)/wedge-shaped LTO (t_{LTO} = 0–2.5 nm)/CoFeB (1 nm)/W (0.3 nm)/Ta (1.0 nm)/Ru cap (15 nm) was deposited at RT. The MTJ stack was post-anneaed at 300°C; then the stack was patterned into micrometer-scale ellipsoidal MTJs (area: 39 μm^2) using photolithography, Ar ion milling, and lift-off processes.

The epitaxial growth and the resulting surface structures were confirmed by using reflection high-energy electron diffraction (RHEED). The magnetic hysteresis loops were measured by using a superconducting quantum interference device (SQUID) magnetometer (MPMS, Quantum Design Co.). The film composition was determined by the inductively coupled plasma mass-spectroscopy (ICP-MS) technique. Four-probe resistance with a bias voltage of 10 mV was characterized at RT under an in-plane magnetic field of up to ±2.5 kOe parallel to MgO[110] (along an easy axis of Fe). A TMR ratio (%) is defined as $100\times(R_H - R_L)/R_L$, where R_H (R_L) indicates the highest resistance (lowest resistance) in the resistance-magnetic field curve. The electron flow direction from the top to bottom electrode is defined as the positive bias.

3. Results and discussion

3.1 Magnetic properties including interface PMA

The middle panels of Fig. 1 show the RHEED patterns of the Cr, MgO, and LTO surfaces (incident electron beam: parallel to the MgO[100] azimuth). The clear streaks indicate the epitaxial growth of Cr(001), MgO(001), and LTO(001) layers. Moreover, the RHEED patterns reveal that the LTO layer possesses a rock-salt-like structure due to the absence of the spinel superlattices.

The atomic ratio of the LTO was determined to be Li:Ti ~ 4:5 by ICP-MS, almost identical to the target compostion. Note that, when a 30 nm thick LTO film with a spinel structure was epitaxially grown on a MgO(001) substrate using a substrate temperature of 800°C, the LTO resistivity was approximately 1 Ω·cm.

Figure 2 shows the magnetic hysteresis loops with t_{CFB} = 1.1 nm at different PA temperatures. The red and blue curves correspond to out-of-plane (OP) and in-plane (IP) magnetization processes, respectively. While the LTO/CoFeB heterostructure did not show perpendicular magnetization in the as-grown state, perpendicular magnetization was clearly

observed after PA above 250°C. Assuming that the remanence magnetization for the perpendicular direction is equal to saturation, the PMA energy (K_u) can be estimated by $K_u = H_A/2M_s$, where H_A and M_s are the saturation filed for in-plane direction and the saturation magnetization, respectively. The saturation filed for in-plane direction became maximum after PA of 300°C; the effective PMA energy density K_u^{eff} was estimated to be 1.18 Merg/cm^3 by the area enclosed by the OP and IP curves.

The areal saturation magnetization ($M_s t_{CFB}$) and the areal magnetic anisotropy energy density ($K_u^{eff} t_{CFB}$) as a function of t_{CFB} are plotted in Figs. 2(b) and 2(c), respectively. Ideally, $K_u^{eff} t_{CFB}$ for interface PMA can be written as $K_u^{eff} t_{CFB} = K_i + K_v t_{CFB}$, where K_i and K_v are the interface and volume magnetic anisotropy constants, respectively. The K_v contains strain induced magnetocrystalline anisotropy and shape anisotropy. The $K_u^{eff} t_{CFB}$ vs. t_{CFB} plots show a linear relationship with positive K_i values above $t_{CFB} \sim 1.1$ nm for all the PA conditions. Such a linear relationship is typically observed for various interface PMA systems [10,16,21,33,34]. Thus, the observed finite positive intercept denotes the interface PMA at the LTO(001)/CoFeB interfaces. However, due to the presence of a magnetic dead-layer at the interfaces of the CoFeB layer, the magnetically alive CoFeB thickness to determine K_i should be defined by subtracting the dead-layer thickness from the nominal CoFeB thicknesses (t_{CFB}). The intersection of the $M_s t_{CFB}$ vs t_{CFB} plots with the x-axis of Fig. 2(b) corresponds to the dead-layer thickness, t_{Dead}. The as-grown sample and the samples after PA at 250 and 300°C have a dead-layer thickness about 0.3 nm. After PA of 350°C, the dead-layer thickness increases to 0.45 nm, which can be attributed to interdiffusion between the CoFeB layer and the W layer. The slope of $M_s t_{CFB}$ vs. t_{CFB} indicates the saturation magnetization after subtraction of the effect of the dead-layer (*intrinsic* M_s). The intrinsic M_s increases significantly from ~1200 emu/cm^3 of PA of 300°C or less to 1500 emu/cm^3 of PA of 350°C. This indicates that the significant B diffusion from the CoFeB to the W side occurs, forming CoFe alloys at the LTO interface [35,36]. The increase in the intrinsic M_s of CoFeB can reasonably rule out the possibility of significant Li diffusion from LTO to CoFeB by PA because such Li diffusion can lead to significant reduction in the intrinsic M_s. After subtracting t_{Dead}, K_i is obtained as the value of $K_u^{eff} t_{CFB}$ at ($t_{CFB} - t_{Dead}$) = 0 nm. K_v is calculated from the slope of the linear fit. We observed that K_i increases with increasing the PA temperature. However, after PA of 350°C, the $K_u^{eff} t_{CFB}$ plot for $t_{CFB} < 1.1$ nm in Fig. 2(c) deviates from the linear relationship due to the large negative K_v. Therefore, the maximum K_u^{eff} was observed after PA of 300°C (1.18 Merg/cm^3 at $t_{CFB} = 1.1$ nm). The t_{Dead}, intrinsic M_s, K_i, and K_v using the fitting for $t_{CFB} > 1.1$ nm are summarized in Table 1. Note here that the magnitude of the interface PMA is nearly half of those of CoFeB/MgO [13,14] and Fe/$MgAl_2O_4$ interfaces [18].

The microscopic mechanism for the interface PMA for LTO/CoFeB is presumably understood in the same manner as conventional MgO/Fe, in which the interface PMA is attributed to the hybridization of Fe $3d_{z^2}$ and O $2p_z$ states [37]. The electronic structure variation at the O site of LTO by introducing a small number of charge carriers is likely to be negligible.

3.2 TMR and related properties for MgO/LTO barriers

We performed transport measurement in the current-perpendicular-to-plane direction for an orthogonal-type MTJ with an Fe/MgO/LTO/CoFeB structure. The bottom Fe layer has in-plane easy magnetization axis and the top CoFeB layer has perpendicular magnetization due to the strong PMA of the LTO/CoFeB interface. Therefore, the bottom Fe and top CoFeB layers have an orthogonal magnetization configuration at a sufficiently small external magnetic field. The schematics of the magnetization configuration are shown in the inset of Fig. 3(b). The observed TMR ratio is half of the full TMR ratio obtained between perfect parallel and antiparallel configurations [38]. Figure 3(a) shows the t_{LTO} dependence of the resistance area (*RA*) products and *half-TMR* ratios for the MTJs. The half-TMR ratio in this study was defined as follows:

$$\text{Half TMR}(\%) \equiv 100 \times \frac{R(H=0) - R(H=2.5\,\text{kOe})}{R(H=2.5\,\text{kOe})},$$

where $R(H)$ is the resistance of the MTJ. The *RA* increases gradually with increasing t_{LTO} of up to 1.0 nm, obeying the tunneling conduction behavior. However, further increase of t_{LTO} leads to a saturation behavior, in which *RA* is almost independent of t_{LTO}. We confirmed a clear correlation between *RA* and TMR ratios as shown in Figs. 3(a) and 3(b); the TMR ratio decreases with increasing t_{LTO} and reaches almost zero at $t_{LTO} \sim 1.0$ nm, indicating that the transport mechanism through MgO/thick LTO is different from a single MgO or MgO/thin LTO barrier. Note that the saturation filed for in-plane direction detected from the TMR curve shape, is almost independent of t_{LTO}, as shown in Fig. 3(b). Therefore, the PMA energy at the LTO/CoFeB interface is not affected by t_{LTO}. These features indicate that the top region of the LTO layer is electrically conductive for $t_{LTO} > 1.0$ nm, as the exponential increase in *RA* disappears. The vanishing of TMR may be attributed to the formation of the conductive LTO, in which the tunneling mechanism can be much affected by the nature of carrier-mediated transport in the thick LTO region. Another possible reason for the vanishing of TMR is suppression of the Δ_1 coherent tunneling mechanism due to the change in the electronic structure near the band gap. In order to elucidate the dominant transport mechanism through LTO barrier based MTJs, theoretical studies are required.

In the thin LTO region ($t_{LTO} < 1$ nm), there could be the significant effect of interdiffusion of Mg from MgO. Ikhtiar *et al.* reported that a nanometer-thick rock-salt $Mg_{1-x}Ti_xO$ layer is structurally stable and can function as a low *RA* tunnel barrier of MTJs [39]. In addition, rock-salt Li_2MgTiO_4 is known to be insulator or a low conductivity material [40]. We found that polycrystalline heterostructures with LTO/CoFeB show significant Mg diffusion into LTO (see Supplementary Fig. S1). Therefore, it is suggested that at the initial stage of the LTO growth ($t_{LTO} < 1$ nm), diffusion of Mg into LTO

occurs, resulting in insulating properties at the MgO side of the LTO layer. Note that the field dependence of TMR curve does not change clearly. The Mg diffusion, *i.e*., the formation of insulating Mg-doped LTO, has no significant influence on the PMA. This result supports the understanding that regardless of the conductivity of oxide layer, the interface PMA emerges based on the interface hybridization between Fe $3d_{z^2}$ and O $2p_z$ orbitals [37].

4. Summary

By fabricating conductive LTO films epitaxially grown on MgO, the interface PMA was investigated for heterostructures consisting of ferromagnetic CoFeB and conductive rock-salt LTO layers, which can be classified as a new group distinct from metallic multilayers and tunnel junctions. The rock-salt structure was confirmed by RHEED for the 5 nm thick LTO layers. A relatively large interface PMA energy of 1.18 Merg/cm^3 was observed after post-annealing above 250°C. The t_{LTO} dependences of the *RA* and TMR ratio revealed the formation of an electrically conductive LTO in the LTO/CoFeB heterostructures. In actual devices, the LTO will be utilized as a stack of pinned-CoFeB/MgO-barrier/free-CoFeB/PMA-reinforcement-LTO. Replacing the MgO cap layer with LTO in double-MgO MTJs is advantegeous for reducing the device resistance while maintaining a large PMA, which will be suitable for future MRAM applications.

Acknowledgments

This work was partly based on results obtained from a project, JPNP16007, commissioned by the New Energy and Indus-trial Technology Development Organization (NEDO). This work is partly supported by CREST-JST (JPMJCR19J4) and MEXT Initiative to Establish Next-generation Novel Integrated Circuits Centers (X-NICS) (Grant No. JPJ011438). H. K. acknowledges the support of Grant-in-Aid for JSPS Fellows (22J00871).

References

[1] B. Dieny and M. Chshiev, *Rev. Mod. Phys*. **89**, 025008 (2017).
[2] F. Hellman, A. Hoffmann, Y. Tserkovnyak, G. S. D. Beach, E. E. Fullerton, C. Leighton, A. H. MacDonald, D. C. Ralph, D. A. Arena, H. A. Dürr, P. Fischer, J. Grollier, J. P. Heremans, T. Jungwirth, A. V. Kimel, B. Koopmans, I. N. Krivorotov, S. J. May, A. K. Petford-Long, J. M. Rondinelli, N. Samarth, I. K. Schuller, A. N. Slavin, M. D. Stiles, O. Tchernyshyov, A. Thiaville, and B. L. Zink, *Rev. Mod. Phys*. **89**, 025006 (2017).
[3] C. Chappert, A. Fert, and F. N. Van Dau, *Nat. Materials* **6**, 813 (2007).
[4] A. Manchon, J. Železný, I. M. Miron, T. Jungwirth, J. Sinova, A. Thiaville, K. Garello, and P. Gambardella, *Rev. Mod. Phys*. **91**, 035004 (2019).
[5] S. Okamoto, N. Kikuchi, O. Kitakami, T. Miyazaki, Y. Shimada, and K. Fukamichi, *Phys. Rev. B*, **66**, 024413 (2002).
[6] J. Okabayashi, M. A. Tanaka, M. Morishita, H. Yanagihara, and K. Mibu, *Phys. Rev. B*, **105**, 134416 (2022).
[7] H. Onoda, H. Sukegawa, J. Inoue, and H. Yanagihara, *Adv. Mater. Interfaces*, **8**, 2170135 (2021).
[8] C. J. Lin, G. L. Gorman, C. H. Lee, R. F. C. Farrow, E. E. Marinero, H. V. Do, H. Notarys, and C. J. Chien, *J. Magn. Magn. Mater*., **93**, 194 (1991).
[9] J. Okabayashi, Y. Miura, Y. Kota, K. Z. Suzuki, A. Sakuma, and S. Mizukami, *Sci. Rep.,* **10**, 9744 (2020).
[10] S. Ikeda, K. Miura, H. Yamamoto, K. Mizunuma, H. D. Gan, M. Endo, S. Kanai, J. Hayakawa, F. Matsukura, and H. Ohno, *Nat. Mater.*, **9**, 721 (2010).
[11] S. Bhatti, R. Sbiaa, A. Hirohata, H. Ohno, S. Fukami, and S. N. Piramanayagam, *Mater. Today*, **20**, 530 (2017).
[12] K. Nishioka, S. Miura, H. Honjo, H. Inoue, T. Watanabe, T. Nasuno, H. Naganuma, T. V. A. Nguyen, Y. Noguchi, M. Yasuhira, S. Ikeda, and T. Endoh, *IEEE Trans. Electron Devices,* **68**, 2680 (2021).
[13] G.-G. An, J.-B. Lee, S.-M. Yang, J.-H. Kim, W.-S. Chung, and J.-P. Hong, Acta Materialia **87**, 259 (2015).
[14] D. M. Lattery, D. Zhang, J. Zhu, X. Hang, J.-P. Wang, and X. Wang, Scientific Reports **8**, 13395 (2018).
[15] Y. Guo, H. Bai, Q. Cui, L. Wang, Y. Zhao, X. Zhan, T. Zhu, H. Yang, Y. Gao, C. Hu, S. Shen, C. He, and S. Wang, Applied Surface Science **568**, 150857 (2021).
[16] Z. Wen, H. Sukegawa, S. Mitani, and K. Inomata, *Appl. Phys. Lett.*, **98**, 242507 (2011).
[17] J. W. Koo, S. Mitani, T. T. Sasaki, H. Sukegawa, Z. C. Wen, T. Ohkubo, T. Niizeki, K. Inomata, and K. Hono, *Appl. Phys. Lett*., **103**, 192401 (2013).
[18] Q. Xiang, R. Mandal, H. Sukegawa, Y. K. Takahashi, and S. Mitani, *Appl. Phys. Express*, **11**, 063008 (2018).
[19] F. J. A. den Broeder, W. Hoving, and P. J. H. Bloemen, *J. Magn. Magn. Mater.*, **93**, 562 (1991).
[20] J. Koba and K. Kita, *ECS Trans.*, **58**, 127 (2013).
[21] S. Kobayashi, H. Koizumi, H. Yanagihara, J. Okabayashi, T. Kondo, T. Kubota, K. Takanashi, and Y. Sonobe, *Phys. Rev. Appl.*, **19**, 064005 (2023).
[22] Y. Iida, Q. Xiang, T. Scheike, Z. Wen, J. Okabayashi, J. Uzuhashi, T. Ohkubo, K. Hono, H. Sukegawa, and S. Mitani, *APL Mater.*, **12**, 111116 (2024).
[23] T. Scheike, Z. Wen, H. Sukegawa, and S. Mitani, *Appl. Phys. Lett.*, **122**, 112404 (2023).
[24] S. Ikeda, J. Hayakawa, Y. Ashizawa, Y. M. Lee, K. Miura, H. Hasegawa, M. Tsunoda, F. Matsukura, and H. Ohno, *Appl. Phys. Lett.*, **93**, 082508 (2008).
[25] T. Maruyama, Y. Shiota, T. Nozaki, K. Ohta, N. Toda, M. Mizuguchi, A. A. Tulapurkar, T. Shinjo, M. Shiraishi, S. Mizukami, Y. Ando, and Y. Suzuki, *Nat. Nanotechnol.*, **4**, 158 (2009).
[26] H. Kubota, S. Ishibashi, T. Saruya, T. Nozaki, A. Fukushima, K. Yakushiji, K. Ando, Y. Suzuki, and S. Yuasa, *J. Appl. Phys.*, **111**, 07C723 (2012).
[27] S. Tsunegi, H. Kubota, S. Tamaru, K. Yakushiji, M. Konoto, A. Fukushima, T. Taniguchi, H. Arai, H. Imamura, and S. Yuasa, *Appl. Phys. Express*, **7**, 033004 (2014).
[28] H. Sato, E. C. I. Enobio, M. Yamanouchi, S. Ikeda, S. Fukami, S. Kanai, F. Matsukura, and H. Ohno, *Appl. Phys. Lett.*, **105**, 062403 (2014).
[29] D. C. Johnston, *J. Low Temp. Phys.*, **25**, 145 (1976).
[30] Y. Liu, J. Lian, Z. Sun, M. Zhao, Y. Shi, and H. Song, *Chem. Phys. Lett.*, **677**, 114 (2017).
[31] R. J. Cava, D. W. Murphy, S. Zahurak, A. Santoro, and R. S. Roth, *J. Solid State Chem.*, **53**, 64 (1984).
[32] T. Scheike, Z. Wen, H. Sukegawa, and S. Mitani, *Appl. Phys. Lett.*, **120**, 032404 (2022).
[33] J. Sinha, M. Hayashi, A. J. Kellock, S. Fukami, M. Yamanouchi, H. Sato, S. Ikeda, S. Mitani, S. H. Yang, S. S. P. Parkin, and H. Ohno, *Appl. Phys. Lett.*, **102**, 242405 (2013).

[34] C. A. Pandey, X. Li, H. Wang, H. Wang, Y. Liu, H. Zhao, Q. Yang, T. Nie, and W. Zhao, *J. Magn. Magn. Mater.*, **511**, 166956 (2020).
[35] D. M. Lattery, D. Zhang, J. Zhu, X. Hang, J. P. Wang, and X. Wang, *Sci. Rep.*, **8**, 13395 (2018).
[36] G. G. An, J. Bin Lee, S. M. Yang, J. H. Kim, W. S. Chung, and J. P. Hong, *Acta Mater.*, **87**, 259 (2015).
[37] A. Hallal, H. X. Yang, B. Dieny, and M. Chshiev, *Phys. Rev. B* **88**, 184423 (2013).
[38] T. Nozaki, A. Koziol-Rachwal, M. Tsujikawa, Y. Shiota, X. Xu, T. Ohkubo, T. Tsukahara, S. Miwa, M. Suzuki, S. Tamaru, H. Kubota, A. Fukushima, K. Hono, M. Shirai, Y. Suzuki, and S. Yuasa, NPG Asia Materials **9**, e451 (2017).
[39] Ikhtiar, S. Kasai, P. H. Cheng, T. Ohkubo, Y. K. Takahashi, T. Furubayashi, and K. Hono, *Appl. Phys. Lett.*, **108**, 242416 (2016).
[40] M. V. V. M. Satya Kishore, S. Marinel, V. Pralong, V. Caignaert, S. D'Astorg, and B. Raveau, *Mater. Res. Bull.*, **41**, 1378 (2006).

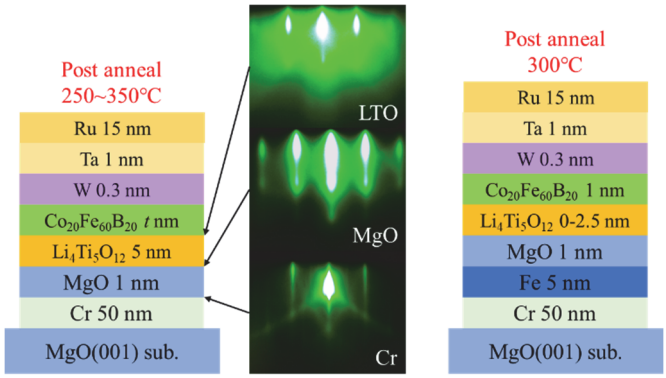

Figure 1. (Left and right) Schematic of multilayer structures prepared for evaluating PMA (left) and orthogonal MTJ (right). (Middle) RHEED patterns for Cr, MgO and LTO layers.

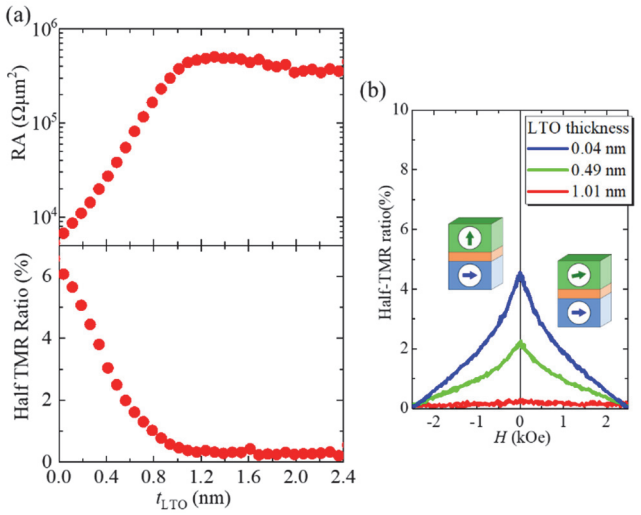

Figure 3. (a) t_{LTO} dependences of *RA* (top) and half TMR ratio (bottom) for Fe/MgO/LTO/CoFeB orthogonal-MTJs. (b) TMR-field curves measured under an in-plane magnetic field.

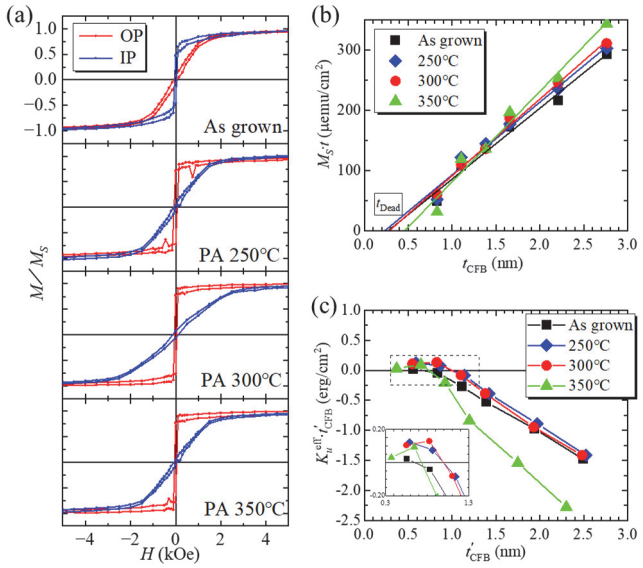

Figure 2. (a) Out-of-plane (OP, red) and in-plane (IP, blue) magnetic hysteresis loops for LTO/CoFeB (t_{CFB} = 1.1 nm) heterostructures as-grown and PA at 250, 300 and 350°C. (b) t_{CFB} dependence of $M_S t_{CFB}$ for different PAs. (c) t'_{CFB} (= t_{CFB} − t_{Dead}) vs. $K_u t'_{CFB}$. The inset of (c) is the close-up of the dashed box.

Table 1. t_{Dead} , intrinsicM_S, K_i and K_v evaluated from the plots for the LTO/CoFeB heterostructures in Fig. 2.

	t_{Dead} (nm)	Intrinsic M_S (emu/cm^3)	K_i (erg/cm^2)	K_v (Merg/cm^3)
As grown	0.27	1180	0.68	−8.63
250°C	0.24	1210	0.91	−9.19
300°C	0.28	1270	0.93	−9.54
350°C	0.46	1500	1.01	−14.48